Deconvolution-Based Partial Volume Correction for Volumetric Blood Flow Measurement

Syed M. Imaduddin, *Student Member, IEEE*, Charles G. Sodini, *Life Fellow, IEEE*, and Thomas Heldt, *Senior Member, IEEE*

Abstract—**Ultrasound-based blood flow (BF) monitoring is vital in the diagnosis and treatment of a variety of cardiovascular and neurologic conditions. Finite spatial resolution of clinical color flow (CF) systems, however, has hampered measurement of vessel cross section areas. We propose a resolution enhancement technique that allows reliable determination of BF in small vessels. We leverage sparsity in the spatial distribution of the frequency spectrum of routinely collected CF data to blindly determine the point spread function (PSF) of the imaging system in a robust manner. The CF data are then deconvolved with the PSF, and the volumetric flow is computed using the resulting velocity profiles. Data were collected from phantom blood vessels with diameters between 2 and 6 mm using a clinical ultrasound system at 2 MHz insonation frequency. The proposed method yielded a flow estimation bias of 0 mL/min, standard deviation of error (SDE) of 22 mL/min, and a root-mean-square error (RMSE) of 22 mL/min over a 150 mL/min range of mean flows. Recordings were also obtained in low signal-to-noise ratio (SNR) conditions using a skull mimicking element, resulting in an estimation bias of −13 mL/min, SDE of 23 mL/min, and an RMSE of 26 mL/min. The effect of insonation frequency was also investigated by obtaining recordings at 4.3 MHz, yielding an estimation bias of −16 mL/min, SDE of 16 mL/min, and an RMSE of 22 mL/min. The results indicate that our technique can lead to clinically acceptable flow measurements across a range of vessel diameters in high and low SNR regimes.**

Index Terms—**Arterial blood flow (BF), color flow (CF), ultrasound, velocity measurements, volumetric BF.**

I. Introduction

ARTERIAL volumetric blood flow (BF) measurement is vital for assessing organ health [1]. In coronary disease treatment, for instance, BF measurement helps determine the need for and success of revascularization procedures [2]. In neuromonitoring applications, BF measurement can help guide the treatment of patients with conditions such as cerebral vasospasms, extracranial and intracranial arterial stenoses,

intracranial hypertension, and traumatic brain injury [3], [4]. BF estimation may also lead to noninvasive estimates of intracranial pressure, elastance, and flow resistance [5]–[7]. Invasive thermodilution or gas exchange techniques are not suitable for continuous BF monitoring, particularly outside an operating room. Imaging modalities such as magnetic resonance angiography (MRA) and positron emission tomography are also not suited for continuous monitoring applications. Ultrasound-based techniques, in contrast, have the potential to provide noninvasive and continuous BF measurement. Such methods, however, have largely been limited to BF monitoring in larger, more superficial vessels (≥ 4 mm diameter) such as the common carotid artery where high-frequency (HF) ultrasound waves (> 4 MHz) can be used to get accurate estimates of vessel cross section areas [8]. For smaller vessels (< 4 mm diameter) deeper inside the body, such as those of the intracranial or coronary circulation, lower ultrasound frequencies (~ 2 MHz) have to be used to overcome increased attenuation. The resulting lack of spatial resolution and unknown aberration-induced perturbation of the point spread function (PSF) leads to poor BF estimates [9]. In such applications, physicians may rely instead on only measuring spatial-maximum/average BF velocity (BFV) [9]–[12]. BFV, however, has been shown to be an imperfect surrogate for BF, and a need persists for reliable, continuous, and noninvasive BF measurement, particularly for smaller vessels deeper inside the body [13].

Color flow (CF) [14] is often used to determine vessel cross section areas that can then be multiplied by BFV estimates derived from spectral Doppler ultrasonongraphy, assuming that BF is well represented by the product of vessel area and BFV. However, commercial ultrasound scanners do not account for subject-specific acoustic attenuation by the underlying tissue, and instead sonographers must adjust the systems' color gain manually to obtain vessel diameter and area measurements. The resulting diameter estimates are therefore user-dependent [15] and may show a significant measurement bias compared with those obtained from methods such as MRA. Wilson *et al.* [9], for instance, reported that while CF-derived middle cerebral artery diameter estimates were correlated with those obtained from MRA, the former were higher by nearly a factor of two. The resulting BF measurements have also been reported to be sensitive to variations in beam-to-vessel angle and rely on the assumption that the vessel cross section is circular [8], [16].

A related measurement approach relies on using 2-D phased arrays or mechanically actuated 1-D array transducers to scan

over the entire vessel cross section [8], [17]–[19]. Mean velocity estimates are computed over the entire lumen and are integrated to yield estimates of the mean BF in an angle-, vessel-geometry-, and flow-profile-independent manner. While this method is calibration-free in principle, it cannot overcome the relatively poor lateral resolution of standard ultrasound transducers. Regions adjacent to a blood vessel also tend to register a nonzero velocity, leading to overestimation of the true flow. Lui and Burns [18] proposed weighting CF power observed at each voxel by the power observed at the vessel center to compensate for this partial insonation effect. Kripfgans *et al.* [8] introduced a similar weighted surface integration method where each voxel was weighted in proportion to its overlap with the estimated vessel lumen. The voxel weights were determined through histogram analysis of the observed CF power. In their original scheme, the authors computed the weights by linearly scaling the CF power. Recently, however, Kripfgans *et al.* [16] suggested that the relationship between true voxel weight and CF power is nonlinear. Moreover, the authors have noted that their method may not be applicable for imaging "small vessels at depth, where high frequency beams are challenged by signal to noise ratio (SNR) and possible aberration effects."

If the PSF of the imaging system is known, the CF power map can be deconvolved to remove the signal leakage. The vessel boundaries can then be determined by standard image processing techniques. Prior work on the application of deconvolution methods to ultrasound imaging has shown, however, that the PSFs are space-varying and may be subject-dependent, thus precluding the use of a single predetermined PSF [20]. Several blind deconvolution approaches have also been proposed that include the use of signal cepstra [21], [22] and higher order signal statistics [23] to estimate the PSF in segments of ultrasound images.

Here, we present a method suitable for BF determination in small vessels (2–4 mm diameter) with low-frequency (LF) (2.3 MHz) CF. Our method relies on deconvolving CF maps to determine the vessel area and velocity profile. Importantly, we show that for CF imaging, the PSF can be estimated by analyzing the CF power spectral density in space. Since fully developed flow profiles encountered in physiological scenarios are near-parabolic, the highest velocity is assumed to occur at a single point within the vessel. The spatial spread of CF power at this velocity therefore serves as an estimate of the PSF. The CF power at the lower velocities can then be deconvolved with this PSF to yield an image with enhanced spatial resolution. The resulting velocity profile can be integrated to yield the volumetric flow. Flow phantom studies were carried out for a range of vessel diameters for two transmission frequencies. The effect of reduced SNR was also investigated using a skull phantom. Our results suggest that our method may be appropriate for BF measurement in vessels including cerebral arteries.

We present our proposed method in Section II and describe our flow phantom setup in Section III. The estimation results are described in Section IV. We then discuss the results in Section V before providing the concluding remarks in Section VI.
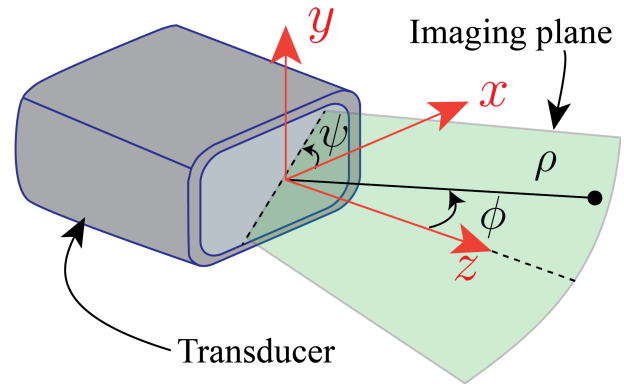

Fig. 1. Coordinate system used in this study. The imaging plane may be rotated about the *z*-axis by an angle ψ. Coordinates within the imaging plane are given by (ρ, ϕ) pairs.

II. VOLUMETRIC FLOW MEASUREMENT METHOD

We develop our technique for sequential ultrasound imaging, but note that the method is also applicable to parallel imaging methods [24], [25]. In the current study, volumetric scanning was not possible and only 2-D CF scans were available. As a result, our method could only be validated for vessels with circular cross sections where the vessel–beam angle was known in advance.

We first present a model for the power spectral density (PSD) of the CF data. A technique for estimating the PSF from PSDs is then outlined and used in a deconvolution procedure—deconvolution is performed laterally—to determine the velocity profile within the target blood vessel's lumen. The velocity profile is subsequently integrated to yield the BF.

A. Preliminaries

As shown in Fig. 1, the radial distance along each measurement plane is denoted as ρ, and the corresponding azimuth angle is denoted as ϕ. CF data are acquired by transmitting an ensemble, N, of focused beams in several directions. The transmission center frequency is denoted as f_0, the pulse duration is denoted as T_p, and the pulses are transmitted at a fixed pulse repetition frequency (PRF). The echoes backscattered by static tissue and moving red blood cells are recorded and demodulated into in-phase and quadrature components. The resulting received signal samples from the coordinates (ρ, ϕ, ψ) are denoted as $\widetilde{s}_{\rho,\phi,\psi}[n] = \widetilde{s}^i_{\rho,\phi,\psi}[n] + j\widetilde{s}^q_{\rho,\phi,\psi}[n]$, where $\widetilde{s}^i$ and $\widetilde{s}^q$ denote the in-phase and quadrature components, respectively, and $n \in \{1, \ldots, N\}$ is the ensemble index. Owing to the sequential nature of data acquisition, the ensemble length, N, is kept small and typically varies between 8 and 32. We model the received signal as

$$\widetilde{s}_{\rho,\phi,\psi}[n] = a * \left(C_{\rho,\phi,\psi}[n] + r_{\rho,\phi,\psi}e^{j2\pi f_{\rho,\phi,\psi}n} \right) \qquad (1)$$

where the asterisk denotes the spatial convolution, a is the 3-D PSF of the imaging system, $r_{\rho,\phi,\psi}$ is a complex valued reflectivity function corresponding to flowing red blood cells with (normalized) frequency $f_{\rho,\phi,\psi} \in [-1/2, 1/2]$, and $C_{\rho,\phi,\psi}[n]$ is the signal due to static or slowly moving tissue (clutter) [14], [20]. The reflectivity values, $r_{\rho,\phi,\psi}$, are assumed

to have a random valued magnitude and a random uniformly distributed phase. Red blood cells typically have a small backscattering cross section than the surrounding tissue. This causes $|r|$ to be orders of magnitude below $|C|$ [26]. The signal frequencies are related to the underlying velocities, $v_{\rho,\phi,\psi}$, by

$$f_{\rho,\phi,\psi} = \frac{2f_0}{cf_p} v_{\rho,\phi,\psi} \cos(\theta_{\rho,\phi,\psi}) \qquad (2)$$

where c is the speed of sound ($\approx$1540 m/s in soft tissue), $\theta_{\rho,\phi,\psi}$ is the flow beam angle, and f_p is the PRF [14]. The clutter and signal from blood can be separated if the signal frequency of the latter is higher than the clutter frequencies. A high-pass (wall) filter is applied to $\tilde{s}$ to yield

$$s_{\rho,\phi,\psi}[n] \approx a * r_{\rho,\phi,\psi} e^{j2\pi f_{\rho,\phi,\psi} n}. \qquad (3)$$

We stress here that the expression above is merely an approximation. In practice, particularly near vessel boundaries when using smaller ensembles, the signal strength may be modulated by the clutter removal process. In our approach, we therefore used relatively larger ensembles of 16 and 32. We use a detrending procedure to remove the clutter [27]. A velocity estimate without angle correction can be obtained from s by a correlation-based estimator [28]

$$\hat{v} = \frac{cf_p}{4\pi f_0} \arg\{\Gamma_{ss}(1)\} \qquad (4)$$

where dependence on spatial coordinates has been omitted for notational simplicity, and $\Gamma_{ss}(1)$ is an estimate of the unit-lag autocorrelation of $s[n]$

$$\Gamma_{ss}(1) = \frac{1}{N-1} \sum_{n=1}^{N-1} s^*[n]s[n+1]. \qquad (5)$$

Here, the superscript asterisk denotes complex conjugation [14]. Also, CF power is defined as

$$P = \frac{1}{N} \sum_{n=1}^{N} |s[n]|^2. \qquad (6)$$

The vessel center, (ρ_t, ϕ_t, ψ_t), can be located by finding the spatial coordinates corresponding to the peak of the frame-averaged CF power.

The velocity profile for all the azimuth angles at the target depth ρ_t can be extracted and is denoted as $\hat{v}_k$, where k is the azimuth index. This process can be repeated for all the rotation angles, ψ, and the resulting velocity profiles can be numerically integrated over ϕ and ψ to determine the volumetric flow. To deal with partial volume effects, Kripfgans et al. proposed using weighted velocity values, $\hat{v}_k \omega_k$, where ω_k is a weight that is determined by analyzing the statistics of the CF power distribution as outlined in Appendix A. The weighted velocity integration procedure proves inadequate when measuring BF in smaller vessels with lower-frequency ultrasound because both vessel areas may be overestimated and the velocity profile may not be faithfully measured. A spatial resolution enhancement procedure is then necessary.

Deconvolution-based resolution enhancement techniques proceed using a measured or estimated PSF to deconvolve the received signals. The deconvolution should ideally be performed in 3-D space. Sequential volumetric data acquisition, however, leads to low frame rates, and thus, conventional sequential ultrasound measurements are made in a 2-D plane (i.e., constant ψ). Deconvolution procedures have been developed, therefore, that operate in two dimensions [29]. Methods have also been proposed that operate only along a single dimension (constant ϕ) [21]. In our approach, to save computational effort, we chose to perform deconvolution only along the azimuth (constant ρ and ψ) leading to a model of the form

$$s_k[n] = a_k * r_k[n] = \sum_l a_{k-l} r_l e^{j2\pi f_l n} \qquad (7)$$

where k and l are the indices of the azimuth, and the PSF is assumed to vary only along the azimuth. We will show that the spatial distribution of the CF frequency spectra is sparse with the highest frequency (velocity) typically close to the vessel center. Here, sparsity implies that the frequency spectra are largely zero, containing energy spikes in regions corresponding to the underlying velocity profiles. We exploit these observations to develop a robust technique to blindly estimate the PSF in a straightforward manner that subsequently allows us to estimate the BF. To do so, we first develop a frequency-domain model for CF data.

B. Frequency-Domain Model of CF Data

We begin by noting that the spatial convolution relationship of (7) applies equivalently in both the time (ensemble) and frequency domains. Equivalently, as shown in Appendix B, computing Fourier transforms of s and r along the time (ensemble) domain

$$S_k(f) = \sum_l a_{k-l} R_l(f) = a_k * R_k(f) \qquad (8)$$

where $S_k(f)$ and $R_k(f)$ are the Fourier transforms of the measured, $s_k[n]$, and actual, $r_k[n]$, CF signals at the kth azimuth, respectively. Here, the measured signals, $s_k[n]$, are the CF signals registered at the kth azimuth and contain effects of the imaging system's PSF, while the term actual signal, $r_k[n]$, refers to the CF signal that would have been obtained from the kth azimuth if a hypothetical system with perfect spatial resolution were used.

PSD measurements may be preferred in sequential measurement applications or in environments with low SNR where the phase information may be unreliable. From (8), the measured PSD at the kth location is

$$\begin{aligned} P_k^S(f) &= \mathbb{E}\{|S_k(f)|^2\} \\ &= \sum_l \sum_m a_{k-l} a_{k-m}^* \mathbb{E}\{R_l(f)R_m(f)^*\} \end{aligned} \qquad (9)$$

where m is an index of the azimuth. Furthermore

$$P_k^S(f) \approx \sum_l |a_{k-l}|^2 \mathbb{E}\{|R_l(f)|^2\} \qquad (10)$$

if $\mathbb{E}\{|R_l(f)|^2\} \gg \mathbb{E}\{R_l(f)R_m(f)^*\}$ for $l \neq m$. Physically, this corresponds to the velocities being nonuniform across the vessel lumen—velocities vary spatially and are not constant
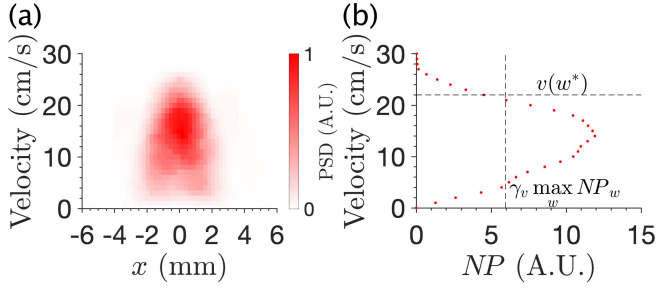
Fig. 2.   (a) Example of a measured PSD map. (b) Normalized power as a function of velocity is plotted and the velocity corresponding to the highest (frequency) velocity index, w^*, is also illustrated.

over space—so that the cross-spectra, $\mathbb{E}\{R_l(f)R_m(f)^*\}$, are small. The resulting PSD model, therefore, is of the form

$$P_k^S(f) \approx |a_k|^2 * P_k^R(f). \tag{11}$$

In summary, the PSD of the CF signal received at the kth azimuth is given by the convolution of the PSD of the underlying CF signals with a space-domain filter with coefficients $|a_k|^2$. In practice, a W-point discrete Fourier transform (DFT) is computed and we arrange the PSD estimates across all K azimuths in a $K \times W$ matrix where

$$\boldsymbol{P^S} = \boldsymbol{AP^R}. \tag{12}$$

Here, $\boldsymbol{A}$ is a $K \times K$ matrix such that

$$\boldsymbol{A} = \begin{bmatrix} |a_0|^2 & |a_{-1}|^2 & \cdots & |a_{-(K-1)}|^2 \\ \vdots & \vdots & \ddots & \vdots \\ |a_{K-1}|^2 & |a_{K-2}|^2 & \cdots & |a_0|^2 \end{bmatrix}. \tag{13}$$

We computed PSDs using the fast Fourier transform (FFT) algorithm for 64 frequency bins ($W = 64$). Ensembles were zero-padded prior to FFT computation. A Hamming window was used for 32-point ensembles to suppress spectral leakage. A rectangular window was used instead for smaller ensembles. Rectangular windows have a more narrow main spectral lobe compared with Hamming windows of the same size allowing us to (partly) compensate for the reduced spectral resolution incurred using the smaller ensemble length [30].

C. PSD Map Recovery

Ideally, the PSD map, $\boldsymbol{P^R}$, is a sparse $K \times W$ matrix, containing nonzero values only at locations inside the vessel lumen at the corresponding frequency (velocity) indices. Our estimation method exploits this sparsity to deconvolve the spectral map, $\boldsymbol{P^S}$. First, the spectral maps from $F = 40$ frames are averaged by computing element-wise medians to reduce noise. The maps are normalized and Gaussian filtering [31] is applied to each frequency band to suppress stochastic variations. A three-stage methodology was developed. In the first stage, the PSF is determined from the measured PSD maps. Next, the PSDs are deconvolved using the estimated PSF. This involves solving an optimization problem, regularized with the sparsity-promoting ℓ_1 norm. The last stage involves postprocessing the deconvolved PSDs to determine the underlying velocity profile.
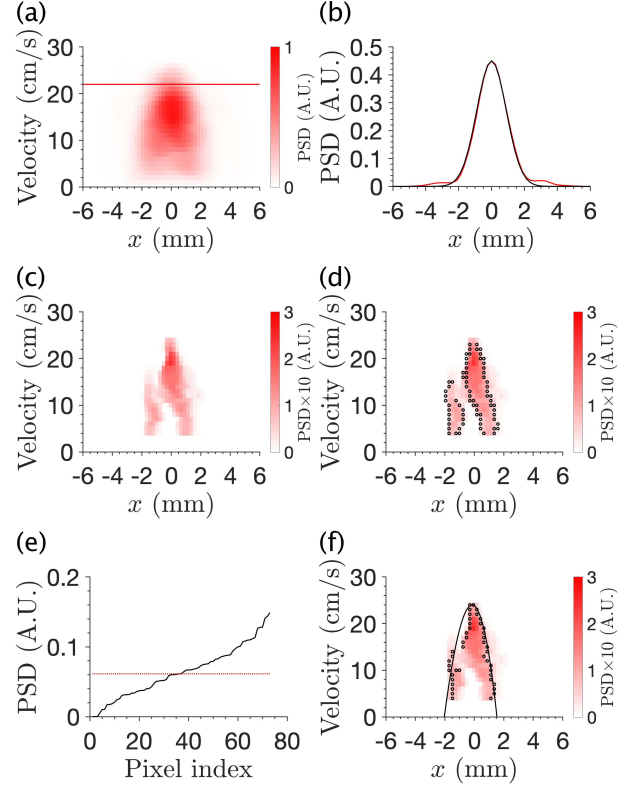

Fig. 3.   (a) Measured PSD map. The row selected for PSF determination is marked in red. (b) PSD spread for the selected row (red) along with the fitted Gaussian (black). (c) Corresponding deconvolved map. (d) Edges detected in the deconvolved map shown in black. (e) PSD values at edges in sorted order (black) and the median (red). (f) Final edge points shown as black dots. The estimated velocity profile is shown in black.

1) PSF Estimation: We assume that in blood vessels far from the aorta, the velocity is uniquely highest at the center of the vessel and drops off toward the vessel wall. Thus, in accordance with (12), the spatial PSD spread at the highest frequency (velocity) is assumed to represent the PSF of the imaging system. Thus, we first need to approximately determine this highest frequency (velocity) before using the corresponding PSD spread as the PSF estimate. To do so, the total (normalized) power as a function of frequency is first determined

$$NP_w = \sum_k \boldsymbol{P^S}_{kw}. \tag{14}$$

The highest frequency (velocity) index is selected such that the normalized power decays to half ($\gamma_v = 0.5$) of its maximum value (see Fig. 2). Moreover, the Otsu image segmentation algorithm [32] is also used to reject background pixels. Fig. 3(a) shows an example of a measured PSD map. The target velocity for PSF determination is marked with a red line. The PSD spread at this target velocity, $\boldsymbol{P^S}_{kw^*}$, is drawn in red in Fig. 3(b) and is used as a surrogate for the 1-D impulse response or PSF of the imaging system. The impulse response itself is modeled as an exponential function of the form

$$a_k = \alpha \exp\left(-\frac{1}{2}|k/\sigma|^p\right) \tag{15}$$

where k is the sample index along the axis, and the parameters, α, σ, and p, are determined by first performing

a nonlinear least-squares curve fit to $\boldsymbol{P}^{S}{}_{kw*}$ [drawn in black in Fig. 3(b)]. We were motivated to choose the model of (15) after observing "Gaussian-like" distributions of PSD values at the detected highest velocities.

2) Deconvolution: Once the PSF has been determined, an estimate, $\widehat{\boldsymbol{A}}$, of the matrix $\boldsymbol{A}$ can be formed and the true underlying frequency map, $\boldsymbol{P}^{R}$, can be estimated [see Fig. 3(c)]. In our application $\boldsymbol{P}^{R}$ is expected to be sparse, and hence the sparsity-promoting ℓ_1 norm was used as a regularization term. We thus estimate $\boldsymbol{P}^{R}$ by solving the optimization problem

$$\widehat{\boldsymbol{P}}^{R} = \arg\min_{\boldsymbol{P}^{R}} J\left(\boldsymbol{P}^{R}\right)$$
$$\text{s.t. } \boldsymbol{P}^{R}{}_{kw} \geq 0 \qquad (16)$$

where $J\left(\boldsymbol{P}^{R}\right)$ is the optimization objective

$$J\left(\boldsymbol{P}^{R}\right) = \|\boldsymbol{P}^{S} - \widehat{\boldsymbol{A}}\boldsymbol{P}^{R}\|_{F}^{2} + \lambda\|\boldsymbol{P}^{R}\|_{1}. \qquad (17)$$

Here, $\|\boldsymbol{P}^{R}\|_{F}^{2}$ is the Frobenius norm of matrix $\boldsymbol{P}^{R}$, defined as the sum of squares of absolute values of $\boldsymbol{P}^{R}$, $\|\boldsymbol{P}^{R}\|_{1}$ is the sum of absolute values of $\boldsymbol{P}^{R}$, and the positivity constraint, $\boldsymbol{P}^{R}{}_{kw} \geq 0$, is imposed since $\boldsymbol{P}^{R}{}_{kw}$ are PSDs. We solved the optimization problem using an alternating direction method of multipliers (ADMM) approach [33]—see Appendix C for a discussion on the computational complexity of the proposed approach.

3) Postprocessing: Once the deconvolved map, $\widehat{\boldsymbol{P}}^{R}$, has been estimated, a velocity profile is determined. The map $\widehat{\boldsymbol{P}}^{R}$ is first binarized. The threshold for this binarization step is determined by examining the boundaries of the map. A Canny edge detector was used for boundary detection [34], and the detected boundaries are illustrated in Fig. 3(d). The median of the PSDs at the map boundaries is used as a subsequent binarization threshold as shown in Fig. 3(e) where the PSD values at the boundaries are shown in black and the resulting median is indicated in red. Thresholds determined in this fashion were found to be more resilient than those determined with other segmentation methods such as the Otsu technique. Pixels where the deconvolved PSD is above this threshold are selected. This is followed by an area opening procedure (7 pixels) to reject spurious detection. Finally, a piecewise-cubic spline is fitted to the edges of the binarized map in a least-squared error sense. This is illustrated in Fig. 3(f) where the outer edges selected using the threshold of Fig. 3(e) are shown as black dots, and the fitted spline that serves as the velocity profile estimate is shown as a black line.

Once the velocity profile has been determined, the volumetric flow can be determined by integrating the profile over all imaging plane angles, ψ. The process can be repeated for more than one depth and the results can be averaged. In our method, we selected depths where the highest CF power at that depth was above 95% of the maximum CF power across all the depths. As in the current study, when the imaging is possible in one plane only, the vessel–transducer angle must be known, and the volumetric flow can be estimated by integrating the velocity profile by assuming the vessel is circular.

III. Flow Phantom Validation

A. Flow Phantom Construction

A flow phantom (see Fig. 4) was constructed to model cardiac and transcranial ultrasound scanning. The system comprised a gear pump (Seaflo, Xiamen, Fujian, China) driven by a motor driver (Dimension Engineering, Hudson, OH, USA). The pump was connected to C-flex tubing (Cole Parmer, Vernon Hills, IL, USA) of varying diameters. For this study, we used tubings of inner diameters (IDs) 2.4, 3.2, 4.0, 4.8, and 6.4 mm. All the tubes had a wall thickness of 0.8 mm with the exception of the 6.4 mm tube that had a 1.6 mm wall thickness. C-flex tubing has previously been used in ultrasound flow phantoms to mimic blood vessels [35]. The tubing was embedded in an agar-based tissue mimicking material mold [36]. Care was taken to keep the vessel segments as straight as possible. This, combined with the dimensions of the flow phantom, allowed us to estimate the vessel angles. Blood mimicking fluid containing suspended nylon particles was circulated through the flow phantom [37]. The mold was designed to mimic cardiac or transcranial insonation, and vessel–beam angles from 20° to 40° could be obtained with transducer–vessel distances of 5–7 cm. A removable Delrin plastic sheet of 1 cm thickness was used to model transcranial insonation and to investigate the effect of reduced SNR on estimation performance. Sound propagates in Delrin at 2430 m/s and is attenuated by 30 dB/cm at 5 MHz [38]. One-way attenuation in the range 5–20 dB, with a mean of 7 dB, was previously reported in four samples of the temporal region of the human skull at 2 MHz [39]. Thus, two-way travel attenuation of 20–40 dB may be expected in transcranial imaging at 2 MHz. Assuming the attenuation in Delrin at 2 MHz is $30/5 \times 2 = 12$ dB/cm, this amounts to two-way attenuation of 24 dB in 1 cm of the plastic layer (i.e., comparable to transcranial attenuation). We found it necessary to perform an aberration correction for results obtained with this skull element in place. The aberration correction strategy is outlined in Appendix D. The flow phantom tubing consisted of a fixed length section of 2.4 mm ID. Two volumetric flow probes (Transonic Systems, Ithaca, NY, USA) were placed around this section of tubing, and the average of their readings was used as the ground truth for volumetric flow following an initial calibration stage in which Transonics measurements were compared with timed-flow measurements.

B. Ultrasound Probe

The Butterfly iQ handheld ultrasound device was used for our experiments [40]. A proprietary software development kit (SDK) was provided by the device manufacturers to export raw in-phase and quadrature demodulated data and allowed for adjustment of transmission and reception parameters. The Butterfly system uses capacitive micromachined ultrasound transducers that allow operation over a wide range of frequencies. Data were collected for an LF stack comprising B-mode and CF images at 1.5 and 2.3 MHz, respectively. Data were also collected in a high-frequency (HF) configuration comprising B-mode images and CF data at 6.5 and 4.4 MHz,

TABLE I
ULTRASOUND TRANSMISSION AND RECEPTION
PARAMETERS FOR (LF) AND (HF)

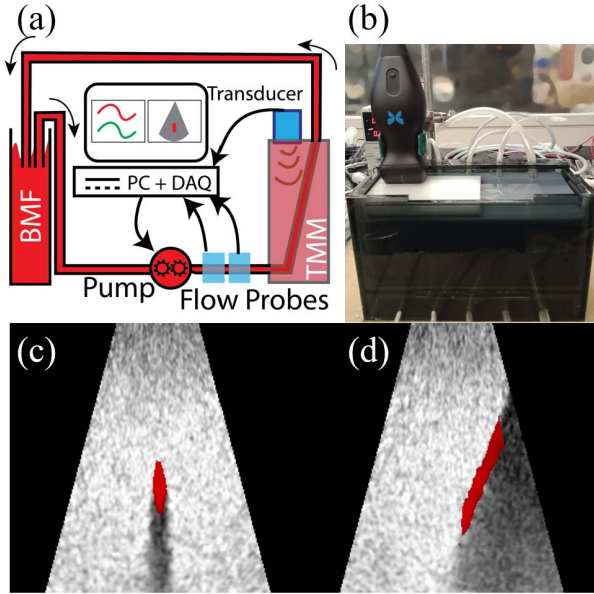| Mode	Parameter	LF	HF
Color Flow	f_0 (MHz)	2.3	4.4
	N	32	
	F# (Reception)	3	
B-Mode	f_0 (MHz)	1.5	6.5
	F# (Reception)	3	

Fig. 4. (a) Flow phantom schematic. BMF: Blood mimicking fluid; TMM: Tissue mimicking material. (b) Flow phantom with skull mimicking element along with examples of CF recordings at (c) $\psi = 0°$ and (d) $\psi = 90°$.

respectively, to investigate frequency dependence of our estimation technique. For the CF modes in each configuration, five-cycle pulses were emitted in ten directions over an 18° span and $K = 88$ multilines were recorded, leading to 0.2° receive line spacing [41]. The reception and transmission parameters are summarized in Table I.

Data were acquired for constant and pulsatile flow without the skull mimicking element for both LF and HF stacks. Measurements were then repeated for the LF stack with the skull element in place. For each tubing, a range of flow rates was generated. The current Butterfly SDK does not allow volumetric CF scanning, and thus, data were collected for two rotation angles, $\psi = 0°$ and $90°$, by manually rotating the probe (see Fig. 4). Velocity profiles across the vessel were determined using the proposed approach, and the volumetric flow was computed following the method of Kripfgans *et al.* by integrating the velocities over a spherical surface passing through the vessel center

$$\dot{Q} = \iint \widehat{v}(\rho_t, \phi, \psi)\rho_t^2 |\sin \phi| d\phi \, d\psi \qquad (18)$$

$$\approx \beta \int \widehat{v}(\rho_t, \phi)\rho_t^2 |\sin \phi| d\phi \qquad (19)$$

where $\widehat{v}$ is the estimated velocity, and ρ_t is the radial distance to the vessel center. The vessel was assumed to be circular, allowing (18) to be approximated as (19) where β is a constant that depends on the transducer–vessel angle, θ, and the measurement plane, ψ

$$\beta = \begin{cases} 1/\cos(\theta), & \psi = 0° \\ \cos(\theta), & \psi = 90° \end{cases} \qquad (20)$$

IV. RESULTS

In total, 104 recordings were obtained with the LF configuration without the skull mimicking element in place. The CF data from all the recordings were processed offline, and the flow measurements were compared against the reference Transonics measurements. For all the experiments, the same set of parameters were used: $W = 64$ DFT points and $\lambda = 0.1$ [see (16)]. The weighted integration approach was also used to determine velocity profiles. The measured lumen extents were compared with known (angle-corrected) values, and the measured average velocities were compared with expected mean velocities.

Examples of the velocity profiles for different tubings are shown in Fig. 5 where the top panel shows overlaid B-mode and CF images for several recordings. The detected vessel centers are indicated with green dots, and the corresponding PSD maps are shown in the bottom panel. Velocity profiles determined both with our approach and with the weighted integration method are also shown, and the resulting volumetric flow measurements are listed. It may be noted that peak velocities determined by our approach are higher than the correlation-based measurements, while the vessel extents determined by our method are smaller. These results demonstrate the need for a deconvolution-based technique for more accurate determination of velocity profiles and volumetric flows.

Fig. 6 shows the Bland–Altman plots for mean velocity, vessel extents, and volumetric flow. Scatter plots are also shown for the volumetric flow measurements along with the corresponding ±20% error bounds. In summary, across all the tubings, the proposed deconvolution method yielded a flow estimation bias of 0 mL/min, standard deviation of error (SDE) of 22 mL/min, and with a root-mean-square error (RMSE) of 22 mL/min over a 150 mL/min range of mean flows. Pearson's correlation coefficient between reference and estimated mean flow measurements was 86%. In contrast, the weighted integration approach yielded a measurement bias of 10 mL/min and SDE of 40 mL/min, with a corresponding RMSE of 41 mL/min with the greatest estimation error accrued for the 2.4 and 3.2 mm tubings. The results are summarized for both the weighted integration approach [see Fig. 7(a)] and our proposed method [see Fig. 7(b)] as a function of tubing diameter. It may be seen that our proposed method exhibits reduced diameter dependence than the weighted integration method.

A. Effect of Reduced SNR

We next obtained 106 recordings for the LF configuration with the skull mimicking element in place to assess the
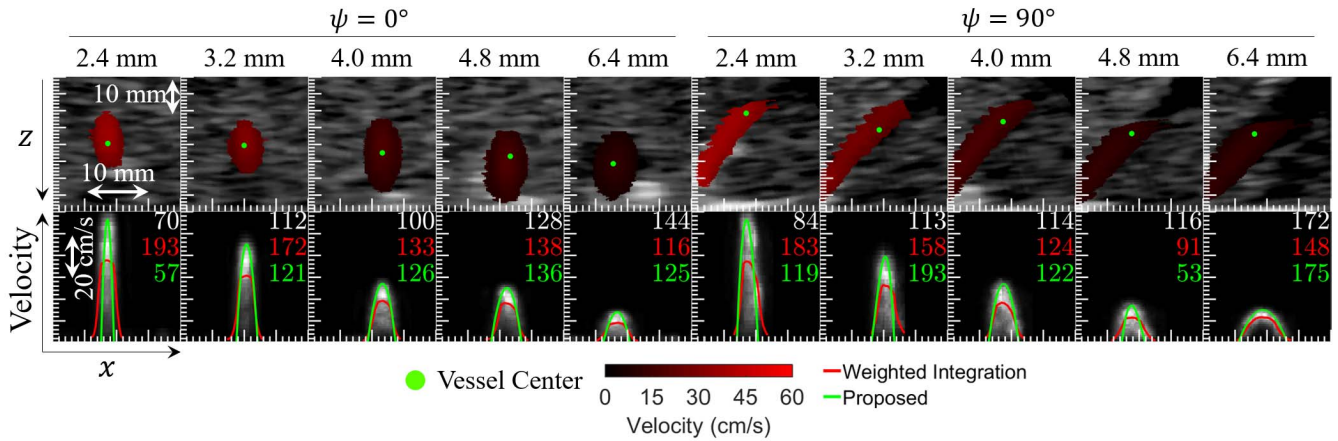
Fig. 5. Examples of CF data and detected vessel centers (green dots) for the LF stack without skull mimicking element. Examples are shown for both $\psi = 0°$ and $90°$. Raw PSD maps are shown. Extracted flow profiles are shown with the weighted integration (red) and proposed (green) methods. The resulting flow rates are also listed along with the reference (white).
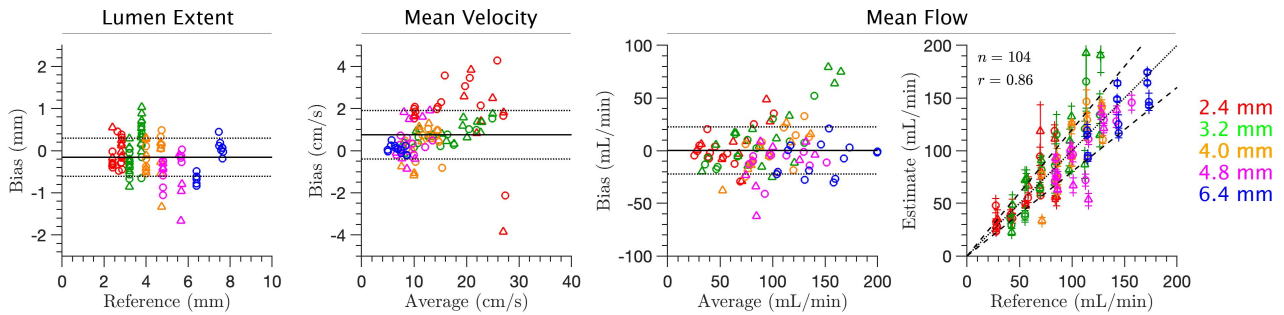

Fig. 6. Bland–Altman and scatter plots for vessel extent, mean velocity, and flow for constant (circles) and pulsatile (triangles) flow with the LF configuration. Bias (solid) and unit SD lines (dotted) are also shown. The mean and unit standard deviation bounds are shown on the scatter plot. Reference lines (dashed) for $\pm 20\%$ flow are also shown in the scatter plot on the right.
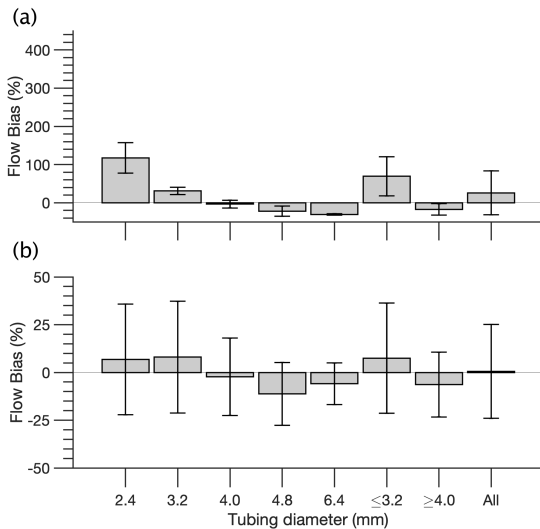

Fig. 7. Per-pipe flow estimation bias and unit standard deviation for (a) weighted integration and (b) the proposed method for the LF configuration without the skull mimicking element.
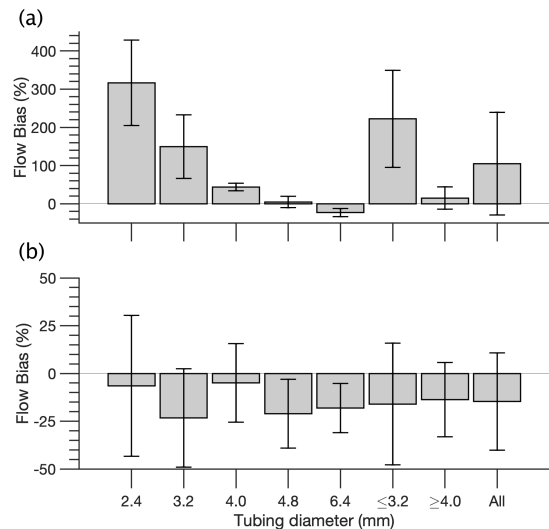

Fig. 8. Per-pipe flow estimation bias and unit standard deviation for (a) weighted integration and (b) the proposed method for the LF configuration with the skull mimicking element.

effect of reduced SNR on the estimation results. Estimates were obtained without altering any hyperparameter. Compared with the measurements without the skull mimicking element, the estimation bias worsened to -13 mL/min and the SDE increased from 22 to 23 mL/min, resulting in an increased RMSE of 26 mL/min. Pearson's correlation coefficient

between reference and estimated mean flow measurements decreased to 79%. The results are summarized in Figs. 8 and 9. Furthermore, the effect of disabling the skull correction option is illustrated in Fig. 10 and shows that the diameters are underestimated in the absence of the aberration correction scheme of Appendix D.
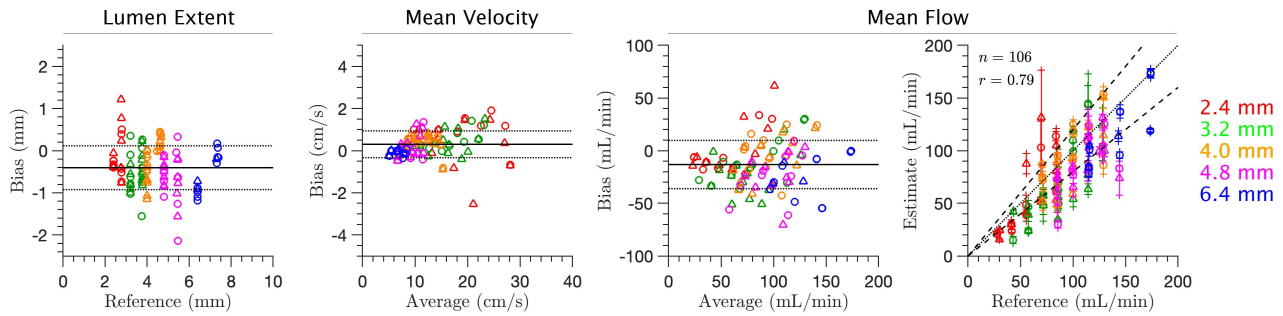
Fig. 9. Bland–Altman and scatter plots for vessel extent, mean velocity, and flow for constant (circles) and pulsatile (triangles) flow for the LF configuration with the skull mimicking element. Bias (solid) and unit SD lines (dotted) are also shown. The mean and unit standard deviation bounds are shown on the scatter plot. Reference lines (dashed) for ±20% flow are also shown in the scatter plot on the right.
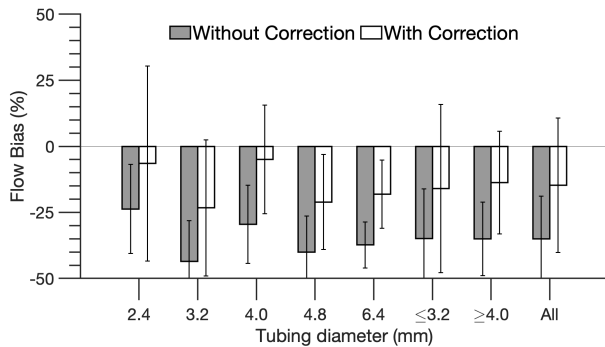

Fig. 10. Effect of disabling skull correction for the LF preset.

B. Effect of Insonation Frequency

Finally, recordings were obtained for the HF configuration. Data collected for the 6.4 mm tubing were found to have a very low SNR due to the larger wall thickness and were thus discarded. The mean flow estimates were obtained in the remaining 87 recordings as before without altering hyperparameters. The qualitative effect of altering the insonation frequency on the imaging resolution was investigated by examining the estimated PSFs. Fig. 11 shows the mean estimated PSFs for the different conditions evaluated here. The results suggest that the estimates are independent of tubing diameters, and that as expected, the PSF widens with lowering frequencies, thereby qualitatively confirming the method's operating principle.

Compared with the measurements with the LF configuration, the flow estimation bias was −16 mL/min, with a significantly reduced SDE of 16 mL/min, resulting in an unchanged RMSE of 22 mL/min. Pearson's correlation coefficient between reference and estimated mean flow measurements remained unchanged at 86%. These results are illustrated in Figs. 12 and 13 and are summarized further in Table II. The negative estimation bias compared with the LF configuration suggests residual dependence on the insonation frequency. This could be addressed in the future by, for instance, tuning the regularization parameter.

C. Sensitivity to Estimation Parameters

The estimation results were computed with varying values of the regularization parameter λ. The results are illustrated in Fig. 14 where it may be seen that the estimation bias starts to become increasingly negative for large values (>0.5) of the regularization parameter. In addition, multi-depth averaging
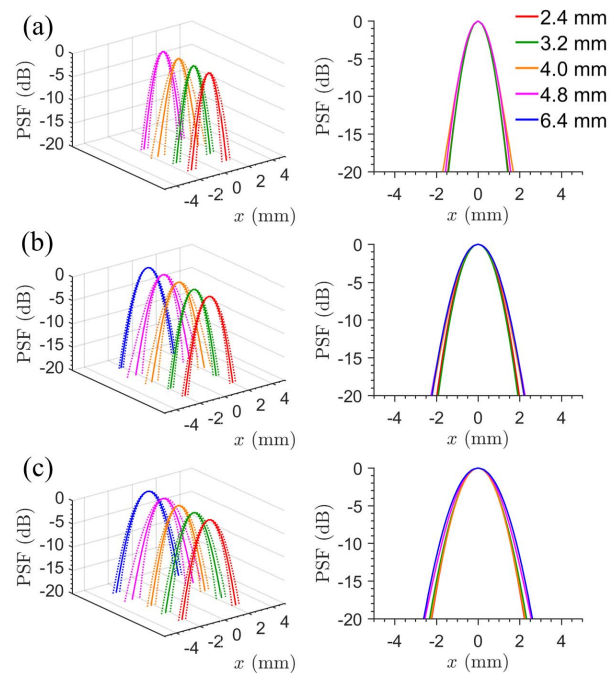

Fig. 11. Mean of estimated PSFs (normalized) for (a) HF and LF stacks (b) without and (c) with the skull along with unit SD bounds (dashed lines). Both 3-D and frontal views are shown. SD bounds removed from frontal views for clarity.

was disabled, and the estimation results were recomputed for only a single depth. For the LF configuration without the skull mimicking element, the RMSE increased from 22 to 24 mL/min, while the bias was −5 mL/min. Similarly, with the skull in place, the RMSE increased to 30 mL/min with a bias of −9 mL/min, while the RMSE changed to 23 mL/min with a bias of −17 mL/min for the HF configuration. Moreover, we altered the velocity selection threshold, γ_v, used to approximately select the highest velocity. The resulting flow estimation bias is shown in Fig. 15 and shows that the estimation bias decreases very slightly with increasing values of γ_v. Finally, the ensemble size was reduced from 32 to 16, and the results were computed by averaging over varying number of frames. The results are shown in Fig. 16 and they show that the estimation results did not change significantly despite the reduced ensemble. Moreover, reducing the number of frames did not lead to estimation degradation. In fact, this helped reduce the estimation bias in certain cases
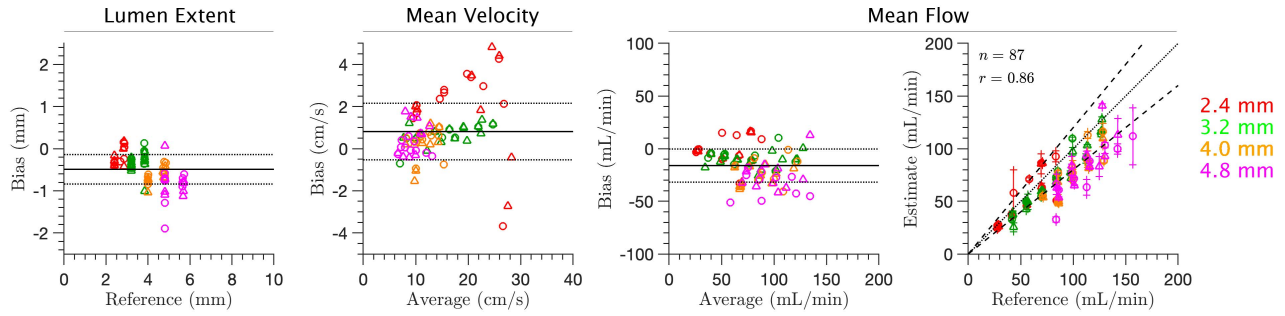
Fig. 12. Bland–Altman and scatter plots for vessel extent, mean velocity, and flow for constant (circles) and pulsatile (triangles) flow for the HF configuration without the skull mimicking element. Bias (solid) and unit SD lines (dotted) are also shown. The mean and unit standard deviation bounds are shown on the scatter plot. Reference lines (dashed) for ±20% flow are also shown in the scatter plot on the right.

TABLE II
ESTIMATION RESULTS' SUMMARY (BIAS, SDE, RMSE)

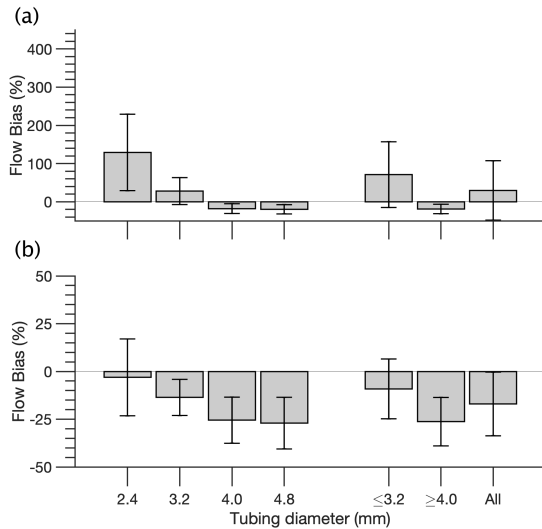|	Stack	Skull	Velocity (cm/s)	Diameter (mm)	Flow (mL/min)	Flow %
Weighted Integration	LF	No	$(-2.3, 1.7, 2.8)$	$(0.2, 1.0, 1.0)$	$(10, 40, 41)$	$(26, 57, 63)$
	LF	Yes	$(4.8, 3.9, 6.2)$	$(0.0, 1.3, 1.2)$	$(65, 70, 95)$	$(105, 134, 170)$
	HF	No	$(-0.7, 3.3, 3.4)$	$(0.0, 0.7, 0.7)$	$(11, 39, 40)$	$(30, 78, 83)$
Proposed	LF	No	$(0.8, 1.2, 1.4)$	$(-0.2, 0.5, 0.5)$	$(0, 22, 22)$	$(1, 25, 24)$
	LF	Yes	$(0.3, 0.6, 0.7)$	$(-0.4, 0.5, 0.7)$	$(-13, 23, 26)$	$(-15, 25, 29)$
	HF	No	$(0.8, 1.3, 1.6)$	$(-0.5, 0.3, 0.6)$	$(-16, 16, 22)$	$(-17, 17, 24)$

Fig. 13. Per-pipe flow estimation bias and unit standard deviation for (a) weighted integration and (b) proposed method for the HF configuration.

(at the potential expense of increased standard deviation in the results).

V. DISCUSSION

A. Flow Estimation Accuracy

Our method achieved RMSEs of 24%, 24%, and 29% for the HF scheme, and for the LF scheme without and with the skull, respectively, in tubings with diameters ranging from 2.4 to 6.4 mm. Prior application of CF-based volumetric flow estimation has largely been limited to major vessels (diameters ~5 mm) [1]. Holland *et al.* [42] previously showed that flow measurement errors with conventional imaging systems could be as high 50% in 3.2 mm diameter vessels and that the error

reduces to 17% for a 12.7 mm diameter vessel. In a more recent study, Hudson *et al.* [15] used the volumetric weighted integration approach to measure flows in porcine abdominal vessels with diameters in the range of 3–6 mm using a Philips 2–7 MHz transducer. Compared with a Transonics flow probe, the derived estimates had a bias of −4.2% with a standard deviation of 10.7% for flows between 60 and 750 mL/min. Kripfgans *et al.* [8], [16] have proposed using weighted velocity integration to overcome partial insonation effects in major vessels. The authors used a wideband 2 to 5 MHz transducer in [8], and a 3.75 MHz transducer in [16]. Recently, they conducted a multi-laboratory investigation of their proposed technique using three different commercial ultrasound scanners [43]. Volumetric flows were measured in a conduit with a mean diameter of 5 mm over a wide range of flows and depth variations. For depths between 2.5 and 5.5 cm and for constant flows, the three scanners had a measurement bias of 4%, −2%, and −23%, respectively, and the measurement standard deviation was seen to degrade for greater depths. Performance, however, was not evaluated for smaller vessels.

We found that the flow estimation accuracy of our implementation of the weighted integration approach showed a diameter dependence, with poorer estimation for diameters below 4 mm [see Fig. 7(a)]. For larger vessels, the estimation error reduced significantly, and the estimated velocity profiles closely followed the ridges in the PSD maps [see Fig. 5]. For smaller vessels, the estimated velocity profile often deviated from the ridge visible in the PSD maps. In some cases, the noise floor setting proved inadequate, leading to significant overestimation. While the noise floor can be raised in such circumstances, the marked deviation of estimated velocities from the PSD map ridges suggests that an alternate approach

may be desirable for recovering the true underlying velocity profile while being resilient to system noise.

The proposed deconvolution-based approach appears feasible for flow estimation in small vessels (<4 mm diameter) using LF (2.3 MHz) ultrasound. The method exhibits reduced diameter dependence compared with the weighted integration approach and yielded volumetric flow estimates with a bias of 0 mL/min and an RMSE of 22 mL/min across a 2–6 mm diameter range at two different measurement angles in both constant and pulsatile flow conditions. Importantly, the estimation was carried out without altering the method's hyperparameters, pointing to the potential robustness of the technique. The estimation accuracy did not degrade substantially (RMSE of 26 mL/min) when the SNR was reduced by introducing a skull mimicking element. Moreover, the estimation performance was also evaluated at a higher frequency (4.4 MHz) without altering the hyperparameters, and while the estimation bias decreased to -16 mL/min, the RMSE did not change due to a reduced SDE.

The estimation bias was close to zero for the LF configuration without the skull mimicking element in place (see Fig. 7). For the remaining configurations, however, the bias was generally negative, indicating flow underestimation. This was potentially caused by diameter underestimation resulting from aggressive deconvolution and can be addressed in the future by, for instance, altering hyperparameters such as the regularization threshold individually for each configuration.

B. Comparison With Prior Deconvolution-Based Methods

Solutions to deconvolution problems can often exhibit sensitivity to changing regularization. Another challenging aspect of deconvolution problems involves the estimation of the PSF. For medical ultrasound imaging, the PSF is known to vary spatially [20] and with changes in acoustic properties of the tissue. Ideally, therefore, the PSF estimates should be space-varying and subject-specific. Classically, deconvolution has been used in medical ultrasound for B-mode resolution enhancement [21], [44]. Recently, a deconvolution-based approach has also been proposed for enhancing the quality of power Doppler images of the microvasculature [45], [46]. In [45], a pretrained PSF was used. At the expense of computing power, not only the Doppler signal but the clutter signals were also estimated. Subsequently, Pham *et al.* [46] proposed a joint-optimization scheme in which deconvolution and PSF estimation were performed iteratively, precluding the need for a pretrained PSF at the cost of increased computation. A single, 2-D, space-invariant PSF was determined for the entire image of interest. The technique was evaluated for imaging the microvasculature using 9 MHz ultrasound with plane wave imaging. Quantitative measurements of flow were not reported. Sensitivity of the results to changes in the regularization parameters was also not reported.

Our proposed technique also relies on deconvolution. The proposed PSF estimation method leverages the observation that the highest velocity occurs at a single point in vessels with fully developed flow. We can approximately isolate the signal from that point by passing the received CF signals
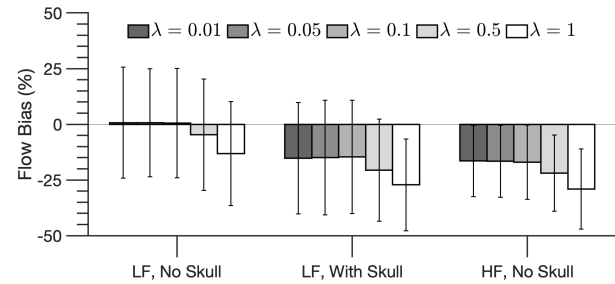

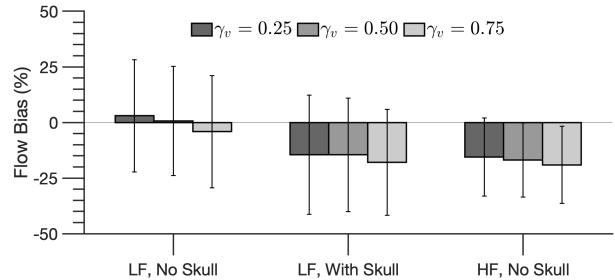Fig. 14. Effect of changing regularization.

Fig. 15. Effect of changing velocity selection threshold, γ_v.

through a passband filter (implemented via PSD estimation). The spatial distribution of the passband filtered signal naturally serves as an estimate of the PSF. The PSFs are inherently space-varying such that separate and possibly different PSFs will be estimated for two vessels at different depths. The proposed technique does not allow estimation of the axial component of the PSF, and thus, estimation accuracy may suffer when using pulses that are longer than the ones evaluated here. The results of our sensitivity analysis show that the estimation results remain comparatively invariant for nearly two orders of magnitude change in the regularization parameter ($0.01 \leq \lambda < 0.5$), pointing to the potential robustness of the technique. For higher values of λ, we found the estimation bias to become increasingly negative (see Fig. 14). We also found that the estimation results were robust to the changes in the velocity selection threshold (see Fig. 15). Importantly, we also found that reducing the ensemble length to 16 did not significantly alter the estimation results. In addition, the results were found to remain consistent when we averaged over fewer frames (see Fig. 16).

C. Features of Our Work

In addition to yielding better estimation accuracy compared with the weighted integration approach, the RMSEs of the estimated vessel extents were 0.6, 0.5, and 0.7 mm across the HF scheme, and for the LF scheme without and with the skull, respectively. This suggests that the underlying mean velocity estimates were also correctly estimated. It is encouraging that these estimation results were obtained across all the tubes and configurations without altering the method's parameters. Moreover, the estimation accuracy does not exhibit as strong a diameter dependence as that of the weighted integration approach (see Figs. 7, 8, and 13) which is also quite encouraging.

Our results suggest that the technique may be appropriate for cerebral arterial BF measurement where the vessels' diameters are of the order of 3 mm [9], [47], [48] and where

(a)

32–Point Ensemble
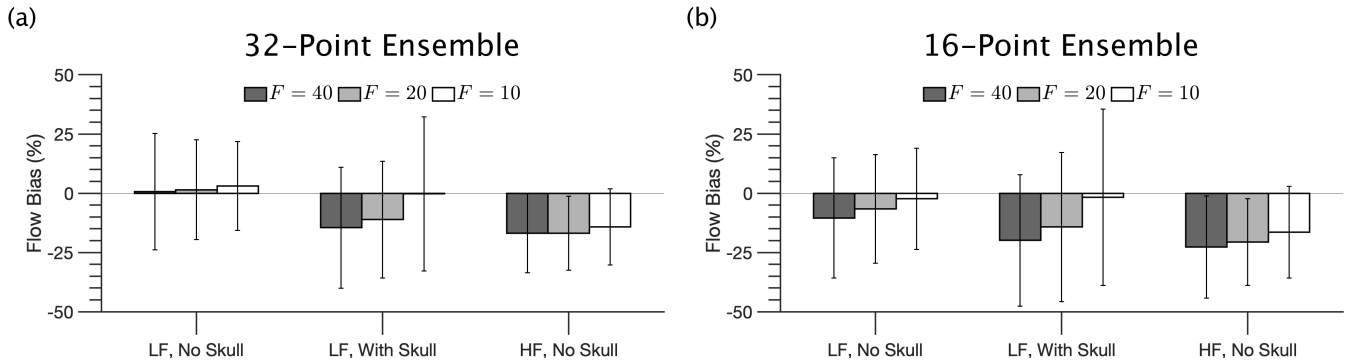
(b)

16–Point Ensemble

Fig. 16. Effect of averaging over multiple frames for ensemble of (a) 32 and (b) 16.

the SNR may be worse compared with that in soft-tissue insonation. In transcranial applications, however, aberration correction may be necessary as evident from Fig. 10 that shows systematic underestimation may occur if the refraction effects of the skull mimicking element are not incorporated. The current skull aberration removal technique applies an approximate correction during data postprocessing. The advantage of this method is that data collected by standard beamforming techniques can be used. Adaptive beamforming techniques, however, will be necessary if greater fidelity is required.

The current work did not explicitly account for spectral broadening [26]. This may be done, for instance, by including a frequency-domain convolution matrix in (12) leading to a model of the form $\boldsymbol{P}^S = \boldsymbol{A}\boldsymbol{P}^R\boldsymbol{\mathcal{W}}$ where a pretrained value for $\boldsymbol{\mathcal{W}}$ may be used.

Demené et al. [49] have recently demonstrated feasibility of imaging cerebral vessels with 2 MHz ultrasound. Their approach, however, requires microbubble infusion. In contrast, the approach proposed here does not require contrast agents and is therefore suitable for long-duration monitoring applications. This comes, naturally, at the expense of imaging resolution that may be obtained with use of contrast agents.

The contributions of our work therefore include the development of a mathematical description for the PSD maps of CF data. A simple technique has been proposed to determine the PSF of the imaging system, and an algorithm has been proposed to deconvolve the PSD maps to obtain velocity profiles. A coordinate mapping technique has also been proposed to account for cranial aberrations. Extensive experiments have been conducted, and the proposed technique has been shown to measure volumetric flows in vessels with diameters as low as 2.4 mm with both 2.3 and 4.4 MHz ultrasound across a range of measurement angles. The proposed algorithm was applied to data from all the frequencies without altering the estimation parameters, pointing to the robustness of the proposed technique. At present, raw radio frequency (RF) signal averaging was not used and could help yield more consistent results, particularly in cases with low SNR.

D. Extension to Physiological Flow Profiles

The proposed PSF estimation method relies on the velocity being higher near the center of the vessel. Such conditions may not always exist in physiological flow profiles encountered in

clinical practice. For instance, there may be plug-like flow during the systolic phase with near-constant velocity across the vessel lumen. In such scenarios, PSF estimation will have to be performed in the diastolic phases where parabolic-like flow may be expected to exist. Moreover, cardiac gating techniques may be used in future work to overcome limitations imposed by interframe PSD averaging used in the current work. Such PSD averaging may not be applicable to vessels with, for instance, plug flow during systole. Advanced clutter rejection techniques may be explored in the future for more accurate estimation of velocities close to the vessel wall that could get contaminated by clutter due to wall-motion. Under certain (patho)physiological conditions, red blood cells are known to form rouleaux. While our method has not been evaluated under such circumstances, the deconvolved PSD map, $\widehat{\boldsymbol{P}}^R$, can be expected to comprise bright spots corresponding to the regions with rouleaux. The ensuing velocity profile estimation method can be expected to function as before as long as the brightness does not vary by multiple orders of magnitude across the vessel lumen.

E. Limitations and Future Work

While we tested our technique on sequentially recorded CF data, the underlying mathematical formulation is also valid for parallel data acquisition schemes where PSD analysis may not be necessary as the model of (8) may be directly applicable. At present, our clinical ultrasound device did not allow volumetric CF, and thus we performed manual angle correction. In clinical use, such manual angle correction can itself introduce errors in the measurement with a 20° error in the measured angle leading to a 6% error in the estimated velocity [50]. It will be desirable, therefore, to use volumetric CF in subsequent work. For instance, sequential scans may be performed along 2-D planes rotated by a range of angles ψ about the z-axis (see Fig. 1). The vessel cross section in each plane may then be analyzed to extract the velocity profile in that plane. The extracted velocity profiles can then be integrated across all the rotation angles ψ to yield the volumetric flow. The resulting BF estimates would be independent of the vessel–beam angle and vessel shape [8]. Moreover, the current study was limited to a flow phantom. A more realistic skull phantom may be used in future work modeling variable thickness, surface contours, and diffraction from the diploe. Alternate vessel mimicking substances may also be used to overcome shadowing caused by the vessels

used in this work (see Fig. 4). Tests can also be conducted on human subjects, with the ground-truth vessel diameters possibly obtained via MRI or CT imaging. Future work can also focus on implementing the algorithm for real-time operation to allow long-term data collection for monitoring applications. In future work, simultaneous M-mode measurements of the vessel diameter under varying flow conditions would be beneficial to independently confirm the diameter values. Work could also be done to evaluate the method's performance on models of stenosed vessels where beam–vessel angles can vary drastically. Moreover, at present the PSF estimates could only be evaluated qualitatively, and future work could include comparisons with ground-truth measurements made with hydrophones.

VI. CONCLUSION

With the proposed approach, we were able to determine volumetric flows in vessels with diameters from 2 to 6 mm using the same set of parameters with different insonation frequencies. Experiments were performed with and without skull mimicking elements at multiple vessel–beam angles. The results suggest that our method remains robust to both changes in insonation frequency and SNR. Thus, the proposed technique could pave the way for reliable volumetric flow measurement in small arteries such as those of the cerebral circulation. Ultrasound measurements are currently limited by the need to have trained ultrasound technicians, and clinical translation of our method would greatly benefit from "smart" ultrasound sensors with automated volumetric vessel scanning and detection capabilities.

APPENDIX A
PARTIAL VOLUME CORRECTION VIA WEIGHTED INTEGRATION

Here, we outline our implementation of the partial volume correction method proposed by Kripfgans *et al.* Specifically, weighted velocity values, $\widehat{v}_k \omega_k$, are generated, where ω_k is a weight that is determined by first computing the mode, P_M (most frequently occurring value), of the corresponding distribution of power values, P_k [8], [16] (see Fig. 17). An upper power threshold, P_T, is then set equal to $\gamma \times P_M$ where γ is set to 0.9 as originally prescribed [8]. In our implementation, we found it necessary to also estimate the power noise floor, NF. The weights in our implementation are then

$$\omega_k = \begin{cases} 0, & P_k \leq \text{NF} \\ \min\left(1, \frac{P_k}{P_T}\right), & \text{otherwise.} \end{cases} \quad (21)$$

We empirically set NF as the 60th percentile of the power values.

APPENDIX B
DERIVATION OF (8)

Applying the DFT along the ensemble dimension to $s_k[n]$

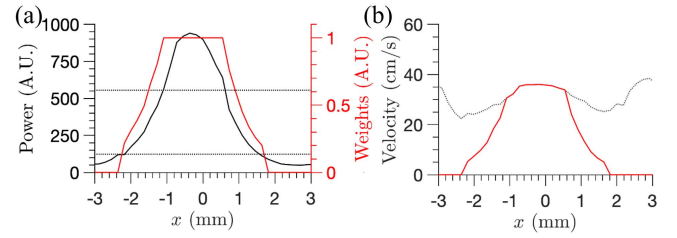$$S_k(f) = \sum_n s_k[n] e^{-j2\pi f n}$$

Fig. 17. Illustration of the method of Kripfgans *et al.* [8]. (a) Velocity weights (red) are determined by analyzing the CF power (black). The process is shown here for a single imaging plane. (b) Raw velocity trace (gray) and weighted velocity profile (red) are shown. Weighted velocity profiles across all the imaging planes are integrated to yield volumetric flow.

$$= \sum_n \left(\sum_l a_{k-l} r_l e^{j2\pi f_l n} \right) e^{-j2\pi f n}$$

$$= \sum_l a_{k-l} \left(\sum_n r_l e^{j2\pi f_l n} e^{-j2\pi f n} \right)$$

$$= \sum_l a_{k-l} R_l(f) = a_k * R_k(f) \quad (22)$$

where $R_k(f) = \sum_n r_k e^{j2\pi f_k n} e^{-j2\pi f n}$. Thus, it may be seen that the spatial convolution relationship between $s_k[n]$ and $r_k[n]$ also applies in the frequency domain between $S_k(f)$ and $R_k(f)$.

APPENDIX C
COMPUTATIONAL ASPECTS OF THE PROPOSED METHOD

Summary: Compared with the approach of Kripfgans *et al.*, the proposed flow estimation procedure is more computationally intensive as it requires computing the PSDs and solving the optimization task of (16). PSD computation was performed using the FFT algorithm. Thus, $\mathcal{O}(KW \log_2 W)$ steps were needed where K is the number of azimuths and W is the number of frequency bins. As shown subsequently, the deconvolution procedure used in the current work required $\mathcal{O}(IK^2W)$ steps, where I is the number of aggregate iterations required in the optimization routine. The optimization method used here can be sped up in the future via parallelization techniques if the current computation cost proves prohibitive for real-time applications.

Derivation: To derive the computational cost of the ADMM approach used here, we begin with the augmented Lagrangian function

$$\mathcal{L} = h(P^R) + \text{tr}\{\Lambda'(P^R - P^Z)\} + \lambda \|P^Z\|_1 + \frac{\zeta}{2} \|P^R - P^Z\|_F^2 \quad (23)$$

where $h(P^R) = \|P^S - \widehat{A}P^R\|_F^2$, tr{} is the trace of a matrix, Λ is a $K \times W$ matrix of Lagrange multipliers, and P^Z is a $K \times W$ set of dummy variables. The iterative procedure of Algorithm 1 was then used.

Here, $J(P^R)$ is the optimization objective function of (17). Step 7 in Algorithm 1 can be performed in an elementwise, closed-form fashion

$$P^Z_{kw} = g\left(\frac{\lambda}{\zeta}, P^R_{kw} - \frac{1}{\zeta}\Lambda_{kw}\right) \quad (24)$$

Algorithm 1 ADMM Procedure

Input: $\widehat{A}, P^S$
Output: $\widehat{P}^R$

  /* Initialization   */
1 $\widehat{P}^R \leftarrow P^S$
2 $P^Z \leftarrow \widehat{P}^R$
3 $\Lambda_{kw} \leftarrow 1 \vee k, w$
4 $\zeta \leftarrow 10$
  /* Optimization   */
5 **while** *Change in* $J(\widehat{P}^R) > 1\%$ **do**
6     $\widehat{P}^R \leftarrow \arg\min_{P^R, P^R_{kw} \geq 0} h(P^R) + \frac{\zeta}{2}\|P^R + \frac{1}{\zeta}\Lambda - P^Z\|_F^2$
7     $P^Z \leftarrow \arg\min_{P^Z} \lambda\|P^Z\|_1 + \frac{\zeta}{2}\|\widehat{P}^R - \frac{1}{\zeta}\Lambda - P^Z\|_F^2$
8     $\Lambda \leftarrow \Lambda + \zeta(\widehat{P}^R - P^Z)$

Algorithm 2 Step 6, Algorithm 1

Input: $\widehat{A}, A_2, X, X_2, P^R_0, \zeta$
Output: $\widehat{P}^R$

  /* Initialization   */
1 $\widehat{P}^R \leftarrow P^R_0$
  /* Optimization   */
2 **while** *Change in* $J_2(\widehat{P}^R) > 0.5\%$ **do**
3   **for** $k = 1 : K$ **do**
4   a $\leftarrow A_{2,kk} + \zeta/2$
5   **for** $w = 1 : W$ **do**
6   b $\leftarrow \frac{\zeta}{2} X_{kw} + X_{2,kw} - \sum_{j,j\neq k} A_{2,kj} \widehat{P}^R_{jw}$
7             $\widehat{P}^R_{kw} \leftarrow \max(0, b/a)$

---

where k and w are the row and column indices, respectively, and $g(a, b)$ is a shrinkage operator [33] defined as

$$g(a, b) = \begin{cases} b - a, & b > a \\ 0, & |b| < a \\ b + a, & b < -a. \end{cases} \tag{25}$$

Thus, Step 7 requires $\mathcal{O}(KW)$ steps as does Step 8.

A coordinate-descent approach was used for Step 6 in Algorithm 1 in which the optimization problem was solved for each element of P^R while holding the remaining elements fixed. Specifically, the objective function in Step 6 is

$$J_2(P^R) = h(P^R) + \frac{\zeta}{2}\|P^R - X\|_F^2 \tag{26}$$

where $X = P^Z - (1/\zeta)\Lambda$. The gradient of J_2 is

$$\frac{\partial J_2}{\partial P^R} = A_2 P^R + \frac{\zeta}{2} P^R - \frac{\zeta}{2} X - X_2 \tag{27}$$

where $A_2 = \widehat{A}^\top \widehat{A}$, and $X_2 = \widehat{A}^\top P^S$. Setting the gradient to zero for the kwth element in P^R and applying the positivity constraint

$$P^R_{kw} = \max(0, b/a)$$
$$a = A_{2,kk} + \zeta/2$$
$$b = \frac{\zeta}{2} X_{kw} + X_{2,kw} - \sum_{j,j\neq k} A_{2,kj} P^R_{jw}. \tag{28}$$

Elements in P^R were iteratively updated using this formulation as shown below in Algorithm 2.

Algorithm 2 requires $\mathcal{O}(I_2 K^2 W)$ where I_2 is the number of iterations of the while loop. Consequently, the ADMM procedure itself requires $\mathcal{O}(I_A I_2 K^2 W)$ where I_A is the number of iterations of the while loop in Algorithm 1. On average, $I = I_A I_2$ is of the order of 50 steps with a maximum of 100.

APPENDIX D
CRANIAL ABERRATION CORRECTION

A cranial aberration correction stage may be needed for transcranial application of our technique. Specifically, the skull is known to defocus transmitted beams, leading to a systematic error in the estimated vessel diameters. Several approaches have been proposed to account for the cranial aberration and
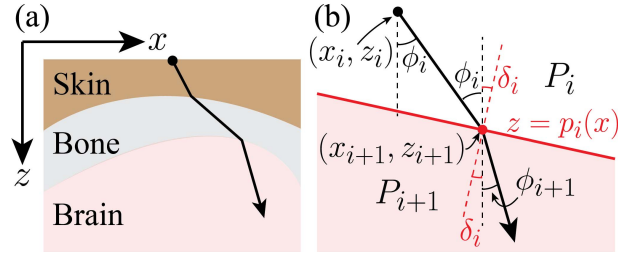

Fig. 18. (a) Model of acoustic transcranial acoustic propagation. Ray refracts at two interfaces. (b) Geometry for one interface is shown.

typically require access to data from individual transducer elements [51]–[53]. These techniques may not be applicable in cases where only postbeamformed data are available as is the case with most commercial devices. In our case, we therefore chose to remap the spatial coordinates of postbeamformed data using ray-theory-based arguments as illustrated in Fig. 18. The skull thickness and position can first be determined using B-mode images (in our case, we manually specified the skull thickness and speed of sound). To account for cranial aberrations, we consider the simplified geometry where two media, P_i and P_{i+1}, are separated by an interface whose coordinates are given by $z = p_i(x)$. The speed of sound in the two media is c_i and c_{i+1}, respectively. A ray originating at (x_i, z_i), moving along the direction ϕ_i in medium P_i, intersects the interface at a coordinate (x_{i+1}, z_{i+1}) and makes an angle $\phi_i + \delta_i$ with the interface normal such that

$$x_{i+1} = x_i + (z_{i+1} - z_i)\tan(\phi_i)$$
$$z_{i+1} = p_i(x_{i+1})$$
$$\delta_i = \tan^{-1}\left(\frac{d}{dx} p_i(x_{i+1})\right)$$
$$\Delta T_i = \frac{1}{c_i}\sqrt{(x_{i+1} - x_i)^2 + (z_{i+1} - z_i)^2} \tag{29}$$

where the interface makes an angle δ_i relative to the z-axis, and ΔT_i is the one-way travel time through the medium. By Snell's law, the ray emerges in medium P_{i+1} with an angle ϕ_{i+1} relative to the z-axis where

$$\phi_{i+1} = \sin^{-1}\left(\frac{c_{i+1}}{c_i}\sin(\phi_i + \delta_i)\right) - \delta_i. \tag{30}$$

Transcranial ultrasound propagation can be modeled using a two-interface geometry [see Fig. 18(a)] where the objective is

to determine corrected coordinates (x', z') for the ultrasound echo received after a one-way travel time T_r, and initially registered as having come from a radial distance $\rho_0 = cT_r$ for a beam transmitted from the origin, $(x_0 = 0, z_0 = 0)$, along initial direction ϕ_0. Then

$$\left(x', z'\right) = \begin{cases} \rho_0(S_0, C_0), & T_r \leq T_0 \\ (x_1, z_1) + \Delta\rho_1(S_1, C_1), & T_0 < T_r \leq T_1 \\ (x_2, z_2) + \Delta\rho_2(S_2, C_2), & T_r > T_1 \end{cases} \quad (31)$$

where $T_i = \Delta T_0 + \cdots + \Delta T_i$, $\Delta\rho_1 = c_s(T_r - T_0)$, $\Delta\rho_2 = c(T_r - T_1)$, and S_i and C_i denote $\sin(\phi_i)$ and $\cos(\phi_i)$, respectively. Here, c and c_s are the speeds of sound in tissue and skull, respectively. The three cases correspond to reflections from regions proximal to the skull, within the skull, and beyond the skull, respectively. The velocity profile estimation and flow computation can proceed as before once the corrected coordinates have been obtained.

ACKNOWLEDGMENT

REFERENCES

[1] F. Forsberg, "Three-dimensional U.S. measurements of blood flow: One step closer to clinical practice," *Radiology*, vol. 296, no. 3, pp. 671–672, Sep. 2020.

[2] S. Vijayan, D. S. Barmby, I. R. Pearson, A. G. Davies, S. B. Wheatcroft, and M. Sivananthan, "Assessing coronary blood flow physiology in the cardiac catheterisation laboratory," *Current Cardiol. Rev.*, vol. 13, no. 3, pp. 232–243, Jul. 2017.

[3] K. F. Lindegaard, T. Lundar, J. Wiberg, D. Sjøberg, R. Aaslid, and H. Nornes, "Variations in middle cerebral artery blood flow investigated with noninvasive transcranial blood velocity measurements," *Stroke*, vol. 18, no. 6, pp. 1025–1030, Nov. 1987.

[4] N. Stocchetti and A. I. R. Maas, "Traumatic intracranial hypertension," *New England J. Med.*, vol. 370, no. 22, pp. 2121–2130, May 2014.

[5] F. M. Kashif, G. C. Verghese, V. Novak, M. Czosnyka, and T. Heldt, "Model-based noninvasive estimation of intracranial pressure from cerebral blood flow velocity and arterial pressure," *Sci. Transl. Med.*, vol. 4, no. 129, p. 129, Apr. 2012.

[6] T. Heldt, T. Zoerle, D. Teichmann, and N. Stocchetti, "Intracranial pressure and intracranial elastance monitoring in neurocritical care," *Annu. Rev. Biomed. Eng.*, vol. 21, no. 1, pp. 523–549, Jun. 2019.

[7] S. M. Imaduddin, A. Fanelli, F. W. Vonberg, R. C. Tasker, and T. Heldt, "Pseudo-Bayesian model-based noninvasive intracranial pressure estimation and tracking," *IEEE Trans. Biomed. Eng.*, vol. 67, no. 6, pp. 1604–1615, Jun. 2020.

[8] O. D. Kripfgans, J. M. Rubin, A. L. Hall, M. B. Gordon, and J. B. Fowlkes, "Measurement of volumetric flow," *J. Ultrasound Med.*, vol. 25, no. 10, pp. 1305–1311, 2006.

[9] M. H. Wilson *et al.*, "Cerebral artery dilatation maintains cerebral oxygenation at extreme altitude and in acute hypoxia—An ultrasound and MRI study," *J. Cerebral Blood Flow Metabolism*, vol. 31, no. 10, pp. 2019–2029, Oct. 2011.

[10] C. A. Giller, M. R. Hatab, and A. M. Giller, "Estimation of vessel flow and diameter during cerebral vasospasm using transcranial Doppler indices," *Neurosurgery*, vol. 42, no. 5, pp. 1076–1081, May 1998.

[11] C. K. Willie *et al.*, "Regional brain blood flow in man during acute changes in arterial blood gases," *J. Physiol.*, vol. 590, no. 14, pp. 3261–3275, Jul. 2012.

[12] C. Imray *et al.*, "Time course variations in the mechanisms by which cerebral oxygen delivery is maintained on exposure to hypoxia/altitude," *High Altitude Med. Biol.*, vol. 15, no. 1, pp. 21–27, Mar. 2014.

[13] R. L. Hoiland and P. N. Ainslie, "CrossTalk proposal: The middle cerebral artery diameter does change during alterations in arterial blood gases and blood pressure," *J. Physiol.*, vol. 594, no. 15, pp. 4073–4075, Aug. 2016.

[14] J. Jensen, *Estimation of Blood Velocities Using Ultrasound: A Signal Processing Approach*. Cambridge, U.K.: Cambridge Univ. Press, 1996.

[15] J. M. Hudson, R. Williams, L. Milot, Q. Wei, J. Jago, and P. N. Burns, "*In vivo* validation of volume flow measurements of pulsatile flow using a clinical ultrasound system and matrix array transducer," *Ultrasound Med. Biol.*, vol. 43, no. 3, pp. 579–585, Mar. 2017.

[16] O. D. Kripfgans, J. M. Rubin, S. Z. Pinter, J. Jago, R. Leichner, and J. B. Fowlkes, "Partial volume effect and correction for 3-D color flow acquisition of volumetric blood flow," *IEEE Trans. Ultrason., Ferroelectr., Freq. Control*, vol. 66, no. 11, pp. 1749–1759, Nov. 2019.

[17] W. Y. Kim, J. K. Poulsen, K. Terp, and N.-H. Staalsen, "A new Doppler method for quantification of volumetric flow: *In vivo* validation using color Doppler," *J. Amer. College Cardiol.*, vol. 27, no. 1, pp. 182–192, Jan. 1996.

[18] G. Y. Lui and P. N. Burns, "The attenuation compensated C-mode flowmeter: A new Doppler method for blood volume flow measurement," in *Proc. IEEE Ultrason. Symp.*, Oct. 1997, pp. 1285–1289.

[19] S. Berg, H. Torp, B. O. Haugen, and S. Samstad, "Volumetric blood flow measurement with the use of dynamic 3-dimensional ultrasound color flow imaging," *J. Amer. Soc. Echocardiogr.*, vol. 13, no. 5, pp. 393–402, 2000.

[20] J. Ng, R. Prager, N. Kingsbury, G. Treece, and A. Gee, "Modeling ultrasound imaging as a linear, shift-variant system," *IEEE Trans. Ultrason., Ferroelectr., Freq. Control*, vol. 53, no. 3, pp. 549–563, Mar. 2006.

[21] T. Taxt, "Comparison of cepstrum-based methods for radial blind deconvolution of ultrasound images," *IEEE Trans. Ultrason., Ferroelectr., Freq. Control*, vol. 44, no. 3, pp. 666–674, May 1997.

[22] O. V. Michailovich and D. Adam, "A novel approach to the 2-D blind deconvolution problem in medical ultrasound," *IEEE Trans. Med. Imag.*, vol. 24, no. 1, pp. 86–104, Jan. 2005.

[23] U. Abeyratne, A. Petropulu, and J. Reid, "Higher order spectra based deconvolution of ultrasound images," *IEEE Trans. Ultrason., Ferroelectr., Freq. Control*, vol. 42, no. 6, pp. 1064–1075, Nov. 1995.

[24] J. A. Jensen, S. I. Nikolov, A. C. H. Yu, and D. Garcia, "Ultrasound vector flow imaging—Part I: Sequential systems," *IEEE Trans. Ultrason., Ferroelectr., Freq. Control*, vol. 63, no. 11, pp. 1704–1721, Nov. 2016.

[25] J. A. Jensen, S. I. Nikolov, A. C. H. Yu, and D. Garcia, "Ultrasound vector flow imaging—Part II: Parallel systems," *IEEE Trans. Ultrason., Ferroelectr., Freq. Control*, vol. 63, no. 11, pp. 1722–1732, Nov. 2016.

[26] R. Cobbold, *Foundations of Biomedical Ultrasound*. London, U.K.: Oxford Univ. Press, 2007.

[27] M. P. Tarvainen, P. O. Ranta-Aho, and P. A. Karjalainen, "An advanced detrending method with application to HRV analysis," *IEEE Trans. Biomed. Eng.*, vol. 49, no. 2, pp. 172–175, Feb. 2002.

[28] C. Kasai, K. Namekawa, A. Koyano, and R. Omoto, "Real-time two-dimensional blood flow imaging using an autocorrelation technique," *IEEE Trans. Sonics Ultrason.*, vol. SU-32, no. 3, pp. 458–464, May 1985.

[29] M. Alessandrini *et al.*, "A restoration framework for ultrasonic tissue characterization," *IEEE Trans. Ultrason., Ferroelectr., Freq. Control*, vol. 58, no. 11, pp. 2344–2360, Nov. 2011.

[30] A. Oppenheim and R. Schafer, *Discrete-Time Signal Processing*, 3rd ed. Upper Saddle River, NJ, USA: Prentice-Hall, 2002.

[31] C. Rasmussen and C. Williams, *Gaussian Processes for Machine Learning*. Cambridge, MA, USA: MIT Press, 2006.

[32] N. Otsu, "A threshold selection method from gray-level histograms," *IEEE Trans. Syst., Man, Cybern.*, vol. SMC-9, no. 1, pp. 62–66, Jan. 1979.

[33] D. Bertsekas, *Nonlinear Programming*. Nashua, NH, USA: Athena Scientific, 2016.

[34] J. Canny, "A computational approach to edge detection," *IEEE Trans. Pattern Anal. Mach. Intell.*, vol. PAMI-8, no. 6, pp. 679–698, Nov. 1986.

[35] C. Banahan, J. P. Hague, D. H. Evans, R. Patel, K. V. Ramnarine, and E. M. L. Chung, "Sizing gaseous emboli using Doppler embolic signal intensity," *Ultrasound Med. Biol.*, vol. 38, no. 5, pp. 824–833, May 2012.

[36] X. Zhou, D. A. Kenwright, S. Wang, J. A. Hossack, and P. R. Hoskins, "Fabrication of two flow phantoms for Doppler ultrasound imaging," *IEEE Trans. Ultrason., Ferroelectr., Freq. Control*, vol. 64, no. 1, pp. 53–65, Jan. 2017.

[37] K. V. Ramnarine, D. K. Nassiri, P. R. Hoskins, and J. Lubbers, "Validation of a new blood-mimicking fluid for use in Doppler flow test objects," *Ultrasound Med. Biol.*, vol. 24, no. 3, pp. 451–459, Mar. 1998.

[38] A. R. Selfridge, "Approximate material properties in isotropic materials," *IEEE Trans. Sonics Ultrason.*, vol. SU-32, no. 3, pp. 381–394, May 1985.

[39] P. Grolimund, *Transcranial Doppler Sonography*. Vienna, Austria: Springer, 1986.

[40] N. Sanchez *et al.*, "An 8960-element ultrasound-on-chip for point-of-care ultrasound," in *IEEE Int. Solid-State Circuits Conf. (ISSCC) Dig. Tech. Papers*, Feb. 2021, pp. 480–482.

[41] A. Ramalli, A. Rodriguez-Molares, J. Avdal, J. D'hooge, and L. Løvstakken, "High-frame-rate color Doppler echocardiography: A quantitative comparison of different approaches," *IEEE Trans. Ultrason., Ferroelectr., Freq. Control*, vol. 67, no. 5, pp. 923–933, May 2020.

[42] C. K. Holland, M. J. Clancy, K. J. W. Taylor, J. L. Alderman, K. Purushothaman, and T. R. McCauley, "Volumetric flow estimation *in vivo* and *in vitro* using pulsed-Doppler ultrasound," *Ultrasound Med. Biol.*, vol. 22, no. 5, pp. 591–603, 1996.

[43] O. D. Kripfgans *et al.*, "Three-dimensional U.S. for quantification of volumetric blood flow: Multisite multisystem results from within the quantitative imaging biomarkers alliance," *Radiology*, vol. 296, no. 3, pp. 662–670, Sep. 2020.

[44] O. Michailovich, A. Basarab, and D. Kouamé, "Iterative reconstruction of medical ultrasound images using spectrally constrained phase updates," in *Proc. IEEE 16th Int. Symp. Biomed. Imag. (ISBI)*, Apr. 2019, pp. 1765–1768.

[45] H. Shen *et al.*, "High-resolution and high-sensitivity blood flow estimation using optimization approaches with application to vascularization imaging," in *Proc. IEEE Int. Ultrason. Symp. (IUS)*, Oct. 2019, pp. 467–470.

[46] D.-H. Pham, A. Basarab, I. Zemmoura, J.-P. Remenieras, and D. Kouamé, "Joint blind deconvolution and robust principal component analysis for blood flow estimation in medical ultrasound imaging," *IEEE Trans. Ultrason., Ferroelectr., Freq. Control*, vol. 68, no. 4, pp. 969–978, Apr. 2021.

[47] D. R. Enzmann, M. P. Marks, and N. J. Pelc, "Comparison of cerebral artery blood flow measurements with gated cine and ungated phase-contrast techniques," *J. Magn. Reson. Imag.*, vol. 3, no. 5, pp. 705–712, Sep. 1993.

[48] J. Verbree, A. Bronzwaer, M. van Buchem, M. Daemen, J. van Lieshout, and M. van Osch, "Middle cerebral artery diameter changes during rhythmic handgrip exercise in humans," *J. Cerebral Blood Flow Metabolism*, vol. 37, no. 8, pp. 2921–2927, Aug. 2017.

[49] C. Demené *et al.*, "Transcranial ultrafast ultrasound localization microscopy of brain vasculature in patients," *Nature Biomed. Eng.*, vol. 5, no. 3, pp. 219–228, Mar. 2021.

[50] R. W. Gill, "Measurement of blood flow by ultrasound: Accuracy and sources of error," *Ultrasound Med. Biol.*, vol. 11, no. 4, pp. 625–641, Jul./Aug. 1985.

[51] K. Shapoori, J. Sadler, A. Wydra, E. Malyarenko, A. Sinclair, and R. Maev, "An ultrasonic-adaptive beamforming method and its application for trans-skull imaging of certain types of head injuries. Part I: Transmission mode," *IEEE Trans. Biomed. Eng.*, vol. 62, no. 5, pp. 1253–1264, May 2015.

[52] C. Jiang *et al.*, "Ray theory-based transcranial phase correction for intracranial imaging: A phantom study," *IEEE Access*, vol. 7, pp. 163013–163021, 2019.

[53] C. Jiang, Y. Li, K. Xu, and D. Ta, "Full-matrix phase shift migration method for transcranial ultrasonic imaging," *IEEE Trans. Ultrason., Ferroelectr., Freq. Control*, vol. 68, no. 1, pp. 72–83, Jan. 2021.

Syed M. Imaduddin (Student Member, IEEE) received the B.S. degree in electrical engineering from the National University of Science and Technology, Islamabad, Pakistan, in 2015, and the S.M. and Ph.D. degrees in electrical engineering and computer science from the Massachusetts Institute of Technology (MIT), Cambridge, MA, USA, in 2018 and 2022, respectively.

He is currently a Postdoctoral Affiliate at MIT. He is interested in biomedical signal and image processing and particularly in their application to brain care. For his doctoral thesis, he developed ultrasound-based neuromonitoring methods, including techniques for volumetric cerebral blood flow measurement. His prior work includes noninvasive intracranial pressure estimation.

Dr. Imaduddin is a member of the IEEE Engineering in Medicine and Biology Society.

Charles G. Sodini (Fellow, IEEE) received the B.S.E.E. degree from Purdue University, West Lafayette, IN, USA, in 1974, and the M.S.E.E. and Ph.D. degrees from the University of California at Berkeley, Berkeley, CA, USA, in 1981 and 1982, respectively.

He was a Member of the Technical Staff at Hewlett-Packard Laboratories, Palo Alto, CA, USA, from 1974 to 1982, where he worked on the design of MOS memory. He joined the faculty of the Massachusetts Institute of Technology (MIT), Cambridge, MA, USA, in 1983, where he is currently the LeBel Professor of electrical engineering. He is also the Co-Founder of the Medical Electronic Device Realization Center, MIT. Along with Prof. Roger T. Howe, he has coauthored an undergraduate text on integrated circuits and devices entitled *Microelectronics: An Integrated Approach*. He also studied the Hong Kong/South China electronics industry in 1996–1997 and has continued to study the globalization of the electronics industry. He was a Co-Founder of SMaL Camera Technologies, Cambridge, MA, USA, a leader in imaging technology for consumer digital still cameras and machine vision cameras for automotive applications. His research interests are focused on medical electronic systems for monitoring and imaging. These systems require the state-of-the-art mixed-signal-integrated circuit and systems with extremely low energy dissipation.

Dr. Sodini has served on a variety of IEEE Conference Committees, including the International Electron Device Meeting where he was the General Chairman in 1989. He has served on the IEEE Electron Device Society Administrative Committee, was the President of the IEEE Solid-State Circuits Society from 2002 to 2004, and was the Chair for the Executive Committee for the VLSI Symposium from 2006 to 2014. He serves on a variety of industry boards.

Thomas Heldt (Senior Member, IEEE) studied physics at Johannes Gutenberg University, Mainz, Germany; at Yale University, New Haven, CT, USA; and at the Massachusetts Institute of Technology (MIT), Cambridge, MA, USA. He received the Ph.D. degree in medical physics from the Harvard-MIT Division of Health Sciences and Technology, MIT, in 2004.

He undertook postdoctoral training at MIT's Laboratory for Electromagnetic and Electronic Systems. Prior to joining the MIT Faculty, he was a Principal Research Scientist with the Research Laboratory of Electronics, MIT. He is currently an Associate Professor of electrical and biomedical engineering at the Department of Electrical Engineering and Computer Science, a Core Faculty Member of the Institute for Medical Engineering and Science, and a Principal Investigator at the Research Laboratory of Electronics. His research interests include signal processing, mathematical modeling, and model identification in support of real-time clinical decision-making, monitoring of disease progression, and titration of therapy, primarily in neurocritical and neonatal critical care. In particular, he is interested in developing a mechanistic understanding of physiologic systems, and in formulating appropriately chosen computational physiologic models for improved patient care. His research is conducted in close collaboration with clinicians from Boston-area hospitals, where he is integrally involved in designing and deploying high-quality data acquisition systems and collecting clinical data.

Dr. Heldt is a member of the IEEE Engineering in Medicine and Biology (EMB) Cardiopulmonary Systems and Physiology-based Engineering Technical Committee, which he chaired in 2018/2019. In 2019 and 2020, he served as an IEEE EMB Distinguished Lecturer and is currently serving as an Associate Editor for the IEEE TRANSACTIONS ON BIOMEDICAL ENGINEERING. He has also served as the Co-Chair and the Chair of the Cardiopulmonary Systems Theme for the IEEE EMB Conference for which he also serves on the Student Paper Competition Committee.